ACS APPLIED NANO MATERIALS

Open Access

www.acsanm.org

Article

Density Functional Theory Study of Engineering TiS_2 Work Function through Intrinsic Defects and Surface Oxidation for Field-Effect Transistors

Yee-Heng Teh, Sheng-Hsiung Hung, Chin-Hsuan Chen, Angus Huang, Jer-Fu Wang, Chih-Piao Chuu, and Horng-Tay Jeng*

Cite This: *ACS Appl. Nano Mater.* 2025, 8, 19840−19851

Read Online

ABSTRACT: TiS_2 is a van der Waals-layered semiconductor while being highly susceptible to interstitial Ti (Ti_i) defects, rendering a high electrical conductivity. Understanding the influence of Ti_i concentration, surface defects, and thickness dependence on its work function is essential for designing TiS_2-based electrodes in field-effect transistor-related applications. In this work, density functional theory is used to investigate the defect, thickness, and substrate effects toward TiS_2 work function. Our results demonstrate that TiS_2 exhibits a remarkably high work function of 5.75 eV. The high work function is slightly reduced to ∼5.6 eV by Ti_i defects and is insensitive to thickness and Ti_i concentration. We further reveal that surface oxidation and chemisorption of Ti-based adparticles are the causes of low measured TiS_2 work function (4.0−4.5 eV) in experiments. On the other hand, the work function of TiS_2 can be enhanced up to ∼6.1 eV by aluminum oxide (Al_2O_3) substrate while slightly lowered by Ti and Al defects. Our work provides valuable guidance toward engineering high-work-function electrodes in the semiconductor industry.

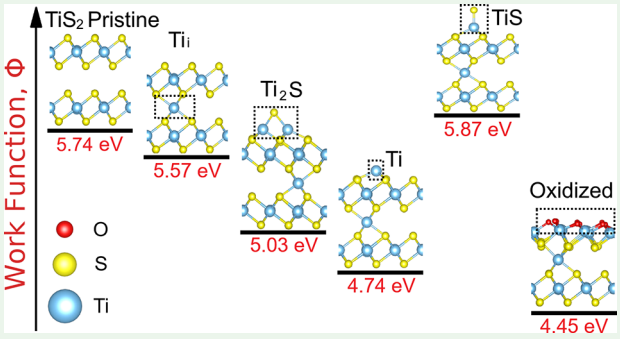

KEYWORDS: *semiconductor, TiS_2, work function, first-principles, 2D materials*

1. INTRODUCTION

Field-effect transistors (FETs) utilize an electric field to control the current flow through the semiconducting channel, enabling energy-efficient and high-speed operations in electronic devices. These transistors consist of three terminals: a source and drain, facilitating, respectively, the entry and exit of charge carriers, and a gate separated from the channel by an insulating gate dielectric. This gate dielectric prevents current flow through the gate while ensuring that the applied gate voltage efficiently modulates the charge carrier concentration in the channel. In pursuit of continuous miniaturization of FETs, conventional metal−oxide−semiconductor field-effect transistors (MOSFETs) are now replacing silicon dioxide as the gate dielectric with high-κ dielectric material such as HfO_2,[1−6] TiO_2,[6−9] and Al_2O_3.[6,7,10,11] The substitution increases the gate capacitance while keeping the leakage current minimal. However, polysilicon, traditionally used as a gate electrode in MOSFETs, is incompatible with high-κ dielectric-based transistors.[12,13] Interaction between the high-κ dielectric and polysilicon gate can lead to significant charge trapping at the interface, thereby causing undesirable threshold voltage deviation (ΔV_{TH}).[13] While using TiN as a metal gate can mitigate the aforementioned issue,[14] its work function may vary depending on the grain orientation,[15] which would also affect the device performance. Furthermore, the reduced channel length associated with miniaturization induces several short-channel effects,[16] including subthreshold leakage current, hot carrier effects, threshold voltage deviation (ΔV_{TH}), direct source-to-drain (S/D) tunneling, punch-through, and carrier mobility degradation.

To address the aforementioned limitations, FETs based on two-dimensional (2D) materials are actively investigated worldwide.[17−21] These materials offer dangling-bond-free surfaces to minimize interface charge trapping, allow easier thickness scaling to simplify miniaturization, and exhibit consistent carrier mobility despite changes in thickness.[22] Among them, graphene is often used as a drain, source, or gate electrode due to its ultrathin layered structure, strong mechanical strength, and high conductivity. However, the use of graphene in electronic devices is constrained by the challenges in scaling up high-quality graphene synthesis as well

Received: July 11, 2025
Revised: October 2, 2025
Accepted: October 3, 2025
Published: October 9, 2025

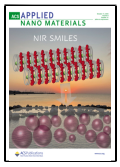

https://doi.org/10.1021/acsanm.5c03229
ACS Appl. Nano Mater. 2025, 8, 19840−19851

as by the presence of a high contact resistance between three-dimensional (3D) metals and graphene. The synthesis of large-area graphene (LAG) is typically achieved via chemical vapor deposition (CVD) on a transition-metal substrate or through epitaxial growth on silicon carbide (SiC).[23] Subsequently, the LAG must be transferred to a target substrate for industrial applications. This transfer process introduces significant challenges, including the risk of mechanical damage (e.g., cracks and wrinkles) and increased production costs.[24] Therefore, exploring alternative 2D metals for use as drain, source, or gate electrodes is crucial in the semiconductor industry.

Titanium disulfide (TiS_2) is a transition-metal dichalcogenide (TMD) 2D material, exhibiting moderately high electrical conductivity.[25] In contrast to the synthesis of LAG, TiS_2 can be synthesized directly on insulating substrates, such as SiO_2/Si via CVD,[26] thereby avoiding the problematic transfer step. To date, TiS_2 nanosheet has been extensively researched as an electrode material in various types of energy devices, including sodium-ion,[27−29] lithium-ion,[30,31] potassium-ion,[32] and magnesium-ion[33] batteries. Recently, Di et al.[34] and Miao et al.[35] successfully employed TiS_2 as a source−drain electrode in a p-type FET, reporting low contact resistance. The semimetallic electronic properties and 2D nature of TiS_2 can effectively mitigate Fermi-level pinning,[36−39] a key mechanism for achieving low contact resistance with semiconductors.

While recent theoretical and experimental studies indicate that pristine TiS_2 is a narrow-band-gap semiconductor, the high conductivity observed in practice is attributed to intrinsic interstitial titanium defects (Ti_i).[25,40] Furthermore, theoretical calculations predict a high work function of approximately 5.7 eV for pristine TiS_2.[41] High-work-function materials are desirable for use as gate electrodes[42,43] and source/drain electrodes in p-type FETs.[44−48] However, experimental measurements of the TiS_2 work function via ultraviolet photon spectroscopy reveal a large discrepancy in values (4.13 eV,[49] 5.3 eV[34]), and the underlying reasons for this discrepancy remain unclear. Notably, the high work function of 5.3 eV was measured on a freshly exfoliated TiS_2 sample, which represents a reasonable approximation for a pristine, low-defect surface. In contrast, surface oxidation is detected on the sample with a lower measured work function (4.13 eV). The discrepancy suggests surface defects crucially affect the work function of TiS_2.

Aluminum oxide (Al_2O_3) is a crucial material in semiconductor processes due to its outstanding thermal stability, excellent electrical insulation, and exceptional mechanical strength, making it indispensable for high-temperature fabrication, current control, and device reliability.[50−52] Its remarkable electrical insulation prevents leakage and ensures precise control of electrical currents in semiconductor devices,[51] and it is widely used as a common substrate (silicon on sapphire) for integrated circuits. Beyond conventional electronics, Al_2O_3 substrates are key for the growth and functionalization of transition-metal dichalcogenides (TMDs), promoting high nucleation densities and two-dimensional film formation, as in WS_2.[53] While small grain sizes can limit charge transport, defect sites can enhance the catalytic performance.[53] In TMD-based FETs, Al_2O_3 acts as a high-κ dielectric, enabling ultrathin films with high on/off ratios and mobility, although surface functionalization or seeding layers are often needed.[54−58] Moreover, Al_2O_3 modulates TMD electronic and optical properties, stabilizes device performance, and supports epitaxial growth of high-quality TMD films.[55,59,60] As mentioned previously, TiS_2, one of the TMD members, has been employed as a source−drain electrode in FETs with low contact resistance;[34,35] hence, in this work, we analyze TiS_2 with aluminum oxide substrate to mimic real applications, as presented in Supporting Information.

In this work, using density functional theory (DFT), we investigate the formation energies of various defects in TiS_2 and their subsequent effect on the work function. We found that Ti_i has a very low defect formation energy and should be the main contributor to intrinsic doping in TiS_2. Although the presence of Ti_i would slightly reduce the work function of pristine TiS_2, the resulting work function is still much higher than the experimental value. Further increasing the Ti_i concentration affects the work function insignificantly. Using TiS_2 with Ti_i defects as the underlying structure, we show that chemisorption of Ti and Ti_2S can have negative defect formation energies at Ti-rich condition. Their highly electropositive attributes would generate negative electric dipole moment at slabs' surface, reducing the work functions to 4.74 and 5.03 eV, respectively. In addition, we demonstrate that with an increasing density of surface oxidation, the TiS_2 work function decreases to 4.45 eV when the surface is fully oxidized. Such an oxidation-suppressed work function provides a reasonable explanation for the experimentally measured lower work function of 4.13 eV.[49] Our study underlies the importance of engineering the surface defect distribution and surface oxidation to control the work function of TiS_2. We also investigate the work function of TiS_2 on the widely used Al_2O_3 substrate. The adsorption behavior of various adparticles including Ti, S, Al, O, and N in the TiS_2/Al_2O_3 system suggests the possibility of atomic intercalation in the heterostructure. The impact of defects on the work function of the TiS_2/Al_2O_3 system is also presented.

2. METHOD

First-principles calculations based on DFT using the Quantum ATK package[61] with norm-conserving pseudopotentials[62] are preformed to study the defect effects on TiS_2. Perdew−Burke−Ernzerhof (PBE) exchange−correlation functional[63] within the generalized gradient approximation (GGA) and Grimmes semiempirical dispersion correction[64] accounting for long-range van der Waals interaction are used in structural optimizations and formation energy calculations. The structures are fully relaxed until the stress of the configurations, max atomic forces, and total energies of the whole systems are converged to 0.1 GPa, 0.025 eV/Å, and 10^{-4} eV, respectively. The density mesh cutoff energy of 3000 eV with $12 \times 12 \times 8$ k-mesh over the Brillouin zone (BZ) is used for pristine bulk TiS_2 calculations; the k-mesh is rescaled appropriately for multilayer or supercell calculations to achieve a similar grid density in BZ. For slab calculations, the optimized bulk lattice parameters and vacuum layer of thickness over 20 Å are adopted, with the atoms of the top/bottom layers relaxed until the forces were converged to 0.025 eV/Å. The electronic structures and work functions are calculated using both the PBE and Heyd−Scuseria−Ernzerhof (HSE) functionals.[65] The screening length 4.81 Å and the exact exchange mixing parameter 0.32 of the HSE functional are employed so that the electronic band gap is in agreement with previous experimental measurements. While the HSE functional is expected to give a more accurate description of electronic structures than the PBE functional, it is much more computationally demanding

https://doi.org/10.1021/acsanm.5c03229
ACS Appl. Nano Mater. 2025, 8, 19840−19851

due to the calculation of the nonlocal Hartree−Fock exchange term. Thus, the auxiliary density matrix method[66] is employed, in which the DFT calculation is performed with a large basis set, while a smaller subset is used to compute Hartree−Fock exchange. Although the HSE functional can yield the correct semiconducting band gap for TiS_2 rather than the metallic behavior given by the standard local density approximation (LDA), the much more computationally demanding HSE calculation is not suitable for the big TiS_2/Al_2O_3 system. Hence, Vienna Ab-initio Simulation Package[67,68] with LDA pseudopotentials is used to study the work function of TiS_2/Al_2O_3.

3. RESULTS AND DISCUSSION

3.1. Structural and Electrical Properties of Bulk TiS_2. We begin with van der Waals-layered TiS_2 in its bulk form. The optimized lattice constants of a = 3.386 Å and c = 5.739 Å are in excellent agreement with experimental values[69] (less than 1.5% deviation). These results are also consistent with previous theoretical work.[70]

Next, we calculate the defect formation energy E_{form} using the conventional method:[71]

$$E_{form} \equiv E_D - E_0 - \Sigma_i n_i \mu_i \quad (1)$$

where E_D is the total energy of the TiS_2 structure with defects; E_0 is the total energy of TiS_2 in the same supercell without defects; and n_i is the number of added (positive) or subtracted (negative) atoms with a chemical potential of μ_i. The chemical potentials μ_{Ti} and μ_S are a range of values that satisfy the equations $(\mu_{Ti} - E_{Ti}) + 2(\mu_S - E_S) = \Delta E(TiS_2)$ and $\mu_{Ti(S)} \leq E_{Ti(S)}$, where E_{Ti} and E_S are the total energies per atom corresponding to the hcp phase of titanium metal and the orthorhombic α phase of bulk sulfur, respectively. Meanwhile, $\Delta E(TiS_2)$ is the formation energy per formula unit of TiS_2 relative to E_{Ti} and E_S, which we calculated to be −4.01 eV, slightly higher than the experimental value of −4.25 eV.[72]

We then investigated the intrinsic defect formation energies of 1T-TiS_2. First, a defect concentration of 3.125% is modeled using a 4 × 4 × 2 supercell, referred to as $Ti_{1.031}S_2$; the intrinsic defects include vacancies and interstitials of Ti (Ti_v and Ti_i) and S (S_v and S_i), the S-on-Ti-antisite (S_{Ti}), and the Ti Frenkel pair (Ti_F) (see Figure S11 for the configurations of intrinsic defects). Given the prior research reported Ti_i concentration as high as 7%,[25] we also analyze the formation energy of 5.56% Ti_i in a 3 × 3 × 2 supercell, referred to as $Ti_{1.056}S_2$ and 6.25% Ti_i in a 4 × 4 × 2 supercell, referred to as $Ti_{1.063}S_2$. Our results shown in Figure 1 are consistent with previous theoretical studies,[40] indicating that Ti_i is the dominant intrinsic defect. Specifically, both $Ti_{1.056}S_2$ and $Ti_{1.031}S_2$ have lower formation energy than all the other non-Ti_i defects within the region between Ti-rich and S-rich conditions. While $Ti_{1.056}S_2$ and $Ti_{1.031}S_2$ exhibit similar formation energies, $Ti_{1.063}S_2$ demonstrates a distinctive trend, exhibiting much lower energies near the Ti-rich region and higher energies otherwise. The distinctive trend arises from the distribution of intercalated Ti: $Ti_{1.063}S_2$ has Ti intercalated between every successive layer, whereas $Ti_{1.031}S_2$ and $Ti_{1.056}S_2$ have Ti intercalated at alternate layers, as shown in Figure S11f,d,g, respectively.

Although the PBE functional yields good structural properties and reliable formation energies, it tends to underestimate the electronic band gaps[73,74] or even erroneously describe narrow-gap materials as semimetals.[75] The band structure of 1T-TiS_2 calculated using the PBE functional (Figure 2a) shows

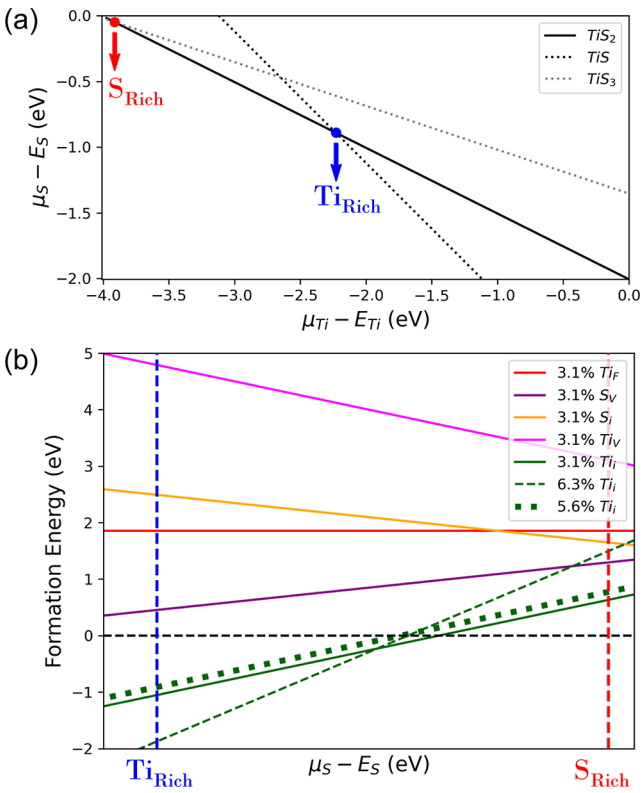

Figure 1. (a) Relationship between the chemical potential of Ti (μ_{Ti}) and S (μ_S) for compounds TiS, TiS_2, and TiS_3, respectively. Chemical potentials between S-rich and Ti-rich conditions represent the thermodynamically stable region of TiS_2, with respect to TiS and TiS_3. (b) Formation energy of intrinsic defects: Ti vacancy (Ti_V), S vacancy (S_V), Ti interstitial (Ti_i), S interstitial (S_i), and Ti Frenkel pairs (Ti_F) in bulk TiS_2 under the condition from Ti-rich to S-rich. Note that TiS_2 with the X concentration of Ti_i is referred to as $Ti_{1.X}S_2$ in the main text.

a metallic state similar to previous study.[70] Using the HSE functional with HSE06 parametrizations[76] (screening length, r_L = 4.81 Å and exact exchange mixing parameter, α = 0.25), we predict a semiconducting electronic band gap of 0.25 eV for pristine TiS_2, which is still lower than the experimental value of ∼0.5 eV based on STS/STM measurements.[40] It should be noted that although α = 0.25 has been rationalized for molecular systems[77] and shown to yield good results for a large range of molecules and semiconductors,[73,77] the optimal α is system- or even property-dependent.[78,79] Thus, in this work, we use a slightly larger value of α = 0.32 in calculating the electronic properties of 1T-TiS_2 and obtain a band gap of 0.48 eV (Figure 2b) close to the experimental value of ∼0.5 eV.[40] The valence band maximum (VBM) is mainly composed of electron orbitals from sulfur, while the conduction band minimum (CBM) of 1T-TiS_2 is composed of electron orbitals from both sulfur and titanium. In addition, we calculate the band gap of 2H−TiS_2 to be 0.63 eV, which rules out the possibility that the high electronic conductivity of TiS_2 measured in experiments[25,40] is attributed to the 2H-polytypes.

3.2. Interstitial Ti and Work Functions. Next, we investigated the work function of pristine TiS_2 as a function of slab thickness. To accurately simulate the decay of charge density into vacuum, the surfaces of TiS_2 were capped with two layers of ghost atoms arranged in 1T-stacking configuration (see Figure S15b for configurations). The work function (Φ) is

https://doi.org/10.1021/acsanm.5c03229
ACS Appl. Nano Mater. 2025, 8, 19840−19851

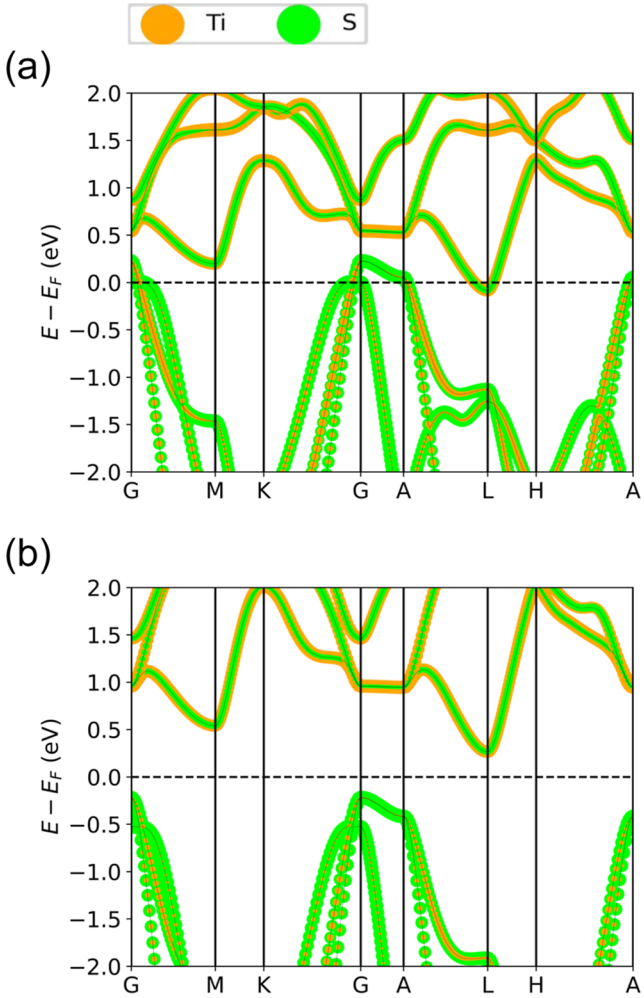

Figure 2. Band structures of pristine bulk 1T-TiS_2 calculated using PBE (a) and HSE (α = 0.32) (b). PBE shows a metallic state, while HSE obtains a semiconducting band gap of 0.48 eV. The VBM is primarily composed of S orbitals, and the CBM (VBM) is composed of both S and Ti orbitals.

calculated by $\Phi = \Phi_{vac} - E_F$, where E_F is the Fermi energy of the slab and Φ_{vac} is the vacuum potential. In this study, Φ_{vac} is calculated from the Poisson equation as

$$\nabla^2 \Phi_{vac}[\delta n](r) = -\frac{e^2}{D(\pi)}\delta n(r) \tag{2}$$

with the electron difference density $\delta n(r)$ being defined through the relation

$$n(r) = \delta n(r) + \sum_{I}^{N_{atom}} n_I(r) \tag{3}$$

where $n(r)$ is the valence electron density obtained from DFT calculations, n_I is the neutral atomic charge density of atom I, and N_{atom} is the number of atoms in the system. Periodic boundary conditions are imposed at the bottom and top of the simulation cell when solving eq 2 to obtain Φ_{vac}. We first analyze the work function of pristine TiS_2 as a function of the film thickness. To enable a consistent comparison of the work function between semiconducting pristine TiS_2 and electron-doped TiS_2 (doped with Ti_i), we align the Fermi level (E_F) to the CBM. The work function significantly increases (Figure 3)

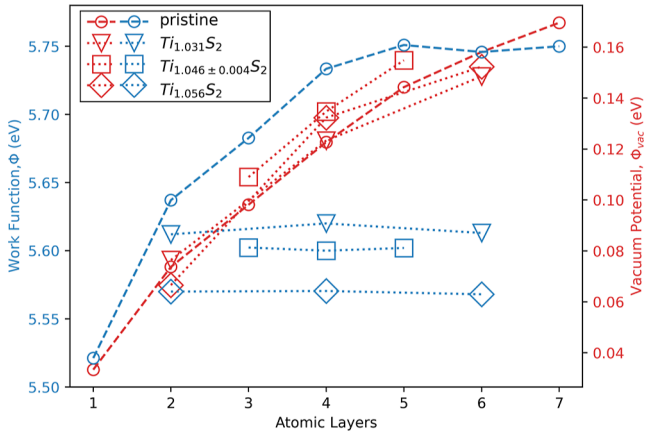

Figure 3. Work functions (Φ) and vacuum potential (Φ_{vac}) of pristine TiS_2 and TiS_2 with Ti_i defects. TiS_2 with 3.125%, 4.6 ± 0.4%, and 5.56% of Ti_i defects are written as $Ti_{1.031}S_2$, $Ti_{1.046\pm0.004}S_2$, and $Ti_{1.056}S_2$, respectively. Note that both $Ti_{1.031}S_2$ (Figure S12a) and $Ti_{1.056}S_2$ (Figure S12c) have similar distributions of Ti_i, i.e., Ti intercalated between every alternate layer, while $Ti_{1.046\pm0.004}S_2$ has Ti intercalated between every successive layer.

with the increasing film thickness up to five atomic layers, primarily due to the decreasing band gap. Above 5 atomic layers, the increase in E_F and Φ_{vac} cancel with each other, and the work function converges to 5.75 eV. We then investigate the work function of $Ti_{1.031}S_2$ (3.125% of Ti_i), $Ti_{1.046\pm0.004}S_2$ (4.6 ± 0.4% of Ti_i), and $Ti_{1.056}S_2$ (5.56% of Ti_i) as a function of slab thickness. Note that both $Ti_{1.031}S_2$ (Figure S12a) and $Ti_{1.056}S_2$ (Figure S12c) have similar distributions of Ti_i, i.e., Ti intercalated between every alternate layer. On the other hand, $Ti_{1.046\pm0.004}S_2$ has Ti intercalated between every successive layer, with the Ti_i concentration of 4.17%, 4.69%, and 5.00% at 3, 4, and 5 atomic layers, respectively. Similar to pristine TiS_2, Φ_{vac} increases with the slab thickness, while the work function remains more or less the same within 1% (5.62 eV−5.57 eV) from 2 to 6 atomic layers for $Ti_{1.031}S_2$, $Ti_{1.046\pm0.004}S_2$, and $Ti_{1.056}S_2$, with the Ti_i concentration nearly doubled (Figure 3). Therefore, we conclude that work functions of TiS_2 are insensitive to variations in the sample thickness.

An examination of the calculated density of states (DOS) in Figure 4 for $Ti_{1.031}S_2$, $Ti_{1.047}S_2$, and $Ti_{1.056}S_2$ (all with 4 layers; see Figure S12 for configurations) reveals that Ti_i acts as an n-type dopant in TiS_2, shifting the Fermi energy (E_F) above the CBM, in agreement with experimental observations.[25] The n-doping caused by Ti_i induces the following changes in the electronic structure: (i) the energies of both the VBM and CBM are reduced; (ii) midgap states are formed between the VBM and CBM, with the main contributions from Ti_i; as the Ti_i concentration increases, the midgap states extend over a broader energy range; (iii) in comparison with the band gap 0.48 eV of a four-layer pristine TiS_2, TiS_2 with Ti_i defects exhibits larger energy gaps between the VBM and CBM, specifically 0.57 eV for $Ti_{1.031}S_2$, 0.56 eV for $Ti_{1.047}S_2$, and 0.62 eV for $Ti_{1.056}S_2$. Interestingly, although n-doping from Ti_i increases E_F by ∼0.1 eV relative to CBM, this increase is relatively insensitive to the Ti_i concentration. Because the surface of TiS_2 is not significantly affected by Ti_i defects, Φ_{vac} remains more or less the same regardless of the Ti_i defect concentration (Figure 3). We conclude that increased Ti_i concentrations only have a minor effect on the work function,

https://doi.org/10.1021/acsanm.5c03229
ACS Appl. Nano Mater. 2025, 8, 19840−19851

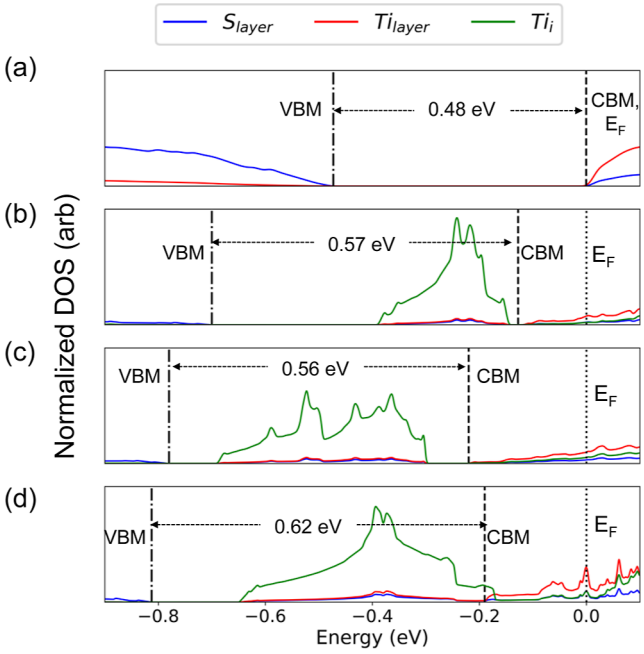

Figure 4. Normalized DOS for 4-layer (a) TiS_2, (b) $Ti_{1.031}S_2$, (c) $Ti_{1.047}S_2$, and (d) $Ti_{1.056}S_2$, projected onto S-layer, Ti-layer, and interstitial Ti (Ti_i) orbitals. The VBM, CBM, and Fermi energy (E_F) are indicated by black dash-dotted, dashed, and dotted lines, respectively. For a better comparison with n-doped cases in (b−d), the Fermi level (E_F) of TiS_2 in (a) has been shifted to CBM.

and thus low measured work functions in experiments cannot be solely explained by Ti_i defects.

3.3. Modulation of Work Function with Adparticles (X = Ti, TiS, and Ti_2S). To study the effects of surface defects on the work function, we employ a two-layer $Ti_{1.031}S_2$ as the underlying structure. We hypothesize that the low formation energy of Ti_i would also facilitate the chemisorption of adparticles (X) consisting of Ti atoms, such as X = Ti, TiS, and Ti_2S. Adparticles (X) are chemisorbed on the top layer of $Ti_{1.031}S_2$ (labeled as X:$Ti_{1.031}S_2$), while the surface of the bottom layer remains as pristine TiS_2 (see Figure S13 for the configurations of surfaces with chemisorbed adparticles).

Since the X:$Ti_{1.031}S_2$ slabs are asymmetric, to solve eq 2, the Dirichlet boundary condition is imposed at the bottom of the simulation cell, setting Φ_{vac} to 0.07 eV (i.e., the vacuum potential of $Ti_{1.031}S_2$ at two atomic layer thickness), while the Neumann boundary condition is imposed at the top of the simulation cell. The calculated formation energies shown in Table 1 reveal that X = Ti, TiS, and Ti_2S are energetically more stable when chemisorbed at hollow sites compared to the top sites of $Ti_{1.031}S_2$. Table 1 demonstrates that the Φ_{vac} values are highly sensitive to the chemisorption of X, while E_F values remain relatively unchanged.

To understand the underlying mechanism driving the changes in Φ_{vac}, we first plot the out-of-plane charge difference profile $\delta n(z)$ (xy-plane-averaged charge difference between the self-consistent charge density and the corresponding neutral atomic charge density) of $Ti_{1.031}S_2$ near the top layer surface, calculated using the HSE functional (see Figure 5a). This plane-averaged $\delta n(z)$ (referred to as $\delta n(z)$) resembles the average electrostatic charge at z, in which positive $\delta n(z)$ represents negative electrostatic charge, or vice versa. Due to the higher electronegativity of sulfur atoms compared to titanium atoms, polar covalent bonds form between the atoms in the Ti-layer and the S_{top}-layer. Consequently, the bonding electron clouds are more localized around the S atoms than the Ti atoms, resulting in a positive $\delta n(z)$ in the region near the S atoms (orange region in Figure 5a). The absence of an adjacent atomic layer above the S_{top}-layer leads to this positive $\delta n(z)$ repelling electrons in its vicinity, creating a negative $\delta n(z)$ region in the vacuum near the S_{top}-layer (blue region in Figure 5a). Subsequently, this negative $\delta n(z)$ region attracts electrons, forming a region of positive $\delta n(z)$ at the outermost vacuum (red region in Figure 5a). This overall charge distribution establishes an inward-pointing negative dipole, which generates positive Φ_{vac} that hinders electrons from leaving the crystal surface.[80]

Next, we plot $\delta n(z)$ of X:$Ti_{1.031}S_2$ with X = Ti, Ti_2S, and TiS, as shown in Figure 5b−d, respectively, and use the plot to estimate Φ_{vac}[81] via

$$\Phi_{vac} = 180.95 \int_0^Z z\delta n(z)\mathrm{d}z + \Phi_{vac(bottom)} \quad (4)$$

In this equation, $-z\delta n(z)$ represents the dipole moment density, z is the height of the simulation cell, and $\Phi_{vac(bottom)}$ is taken as the vacuum potential of $Ti_{1.031}S_2$. Here, the length is expressed in units of Å, energy is expressed in units of eV, and $\int_{z_1}^{z_2} \delta n(z)\mathrm{d}z$ represents the total electrostatic charge from z_1 to z_2, expressed in units of electron number. Equation 4 demonstrates that Φ_{vac} is directly proportional to the integral of the dipole moment density, which is weighted by the distance from the bottom of a simulation cell. While eq 4 tends to overestimate Φ_{vac} (see Table 1), it reliably predicts the relative changes in Φ_{vac} upon chemisorption with X. Specifically: (i) X = Ti and Ti_2S reduce Φ_{vac} to negative values, with chemisorbed Ti inducing a more negative Φ_{vac}; and (ii) X = TiS increases Φ_{vac} to a more positive value.

Table 1. Defect Formation Energies of Chemisorbed Adparticles (X) and Work Functions of the Corresponding Surfaces[a]

adparticles, X	E_{Form} (eV) [Ti-rich]	E_{Form} (eV) [S-rich]	E_F (eV)	Φ_{vac} (eV)	Φ (eV)	Φ_{vac} (eV) [eq 4]
Ti [hollow site]	−0.610	3.640	−5.600	−0.858	4.742	−0.860
Ti_2S [hollow site]	−0.482	1.643	−5.466	−0.441	5.025	−0.441
TiS [hollow site]	0.108	1.170	−5.479	0.392	5.871	0.394
Ti [top site]	0.013	4.263	−5.597	−0.903	4.693	−0.898
Ti_2S [top site]	−0.262	1.863	−5.593	−0.650	4.943	−0.648
TiS [top site]	0.339	1.401	−5.594	0.177	5.771	0.177

[a]The formation energies (E_{Form}) were calculated using the PBE functional for good structural properties. Then, the Fermi energy (E_F), vacuum potential (Φ_{vac}), and work function (Φ) were calculated using the HSE functional for better electronic structures. Vacuum potentials estimated using eq 4 (last column) are included for comparison.

https://doi.org/10.1021/acsanm.5c03229
ACS Appl. Nano Mater. 2025, 8, 19840−19851

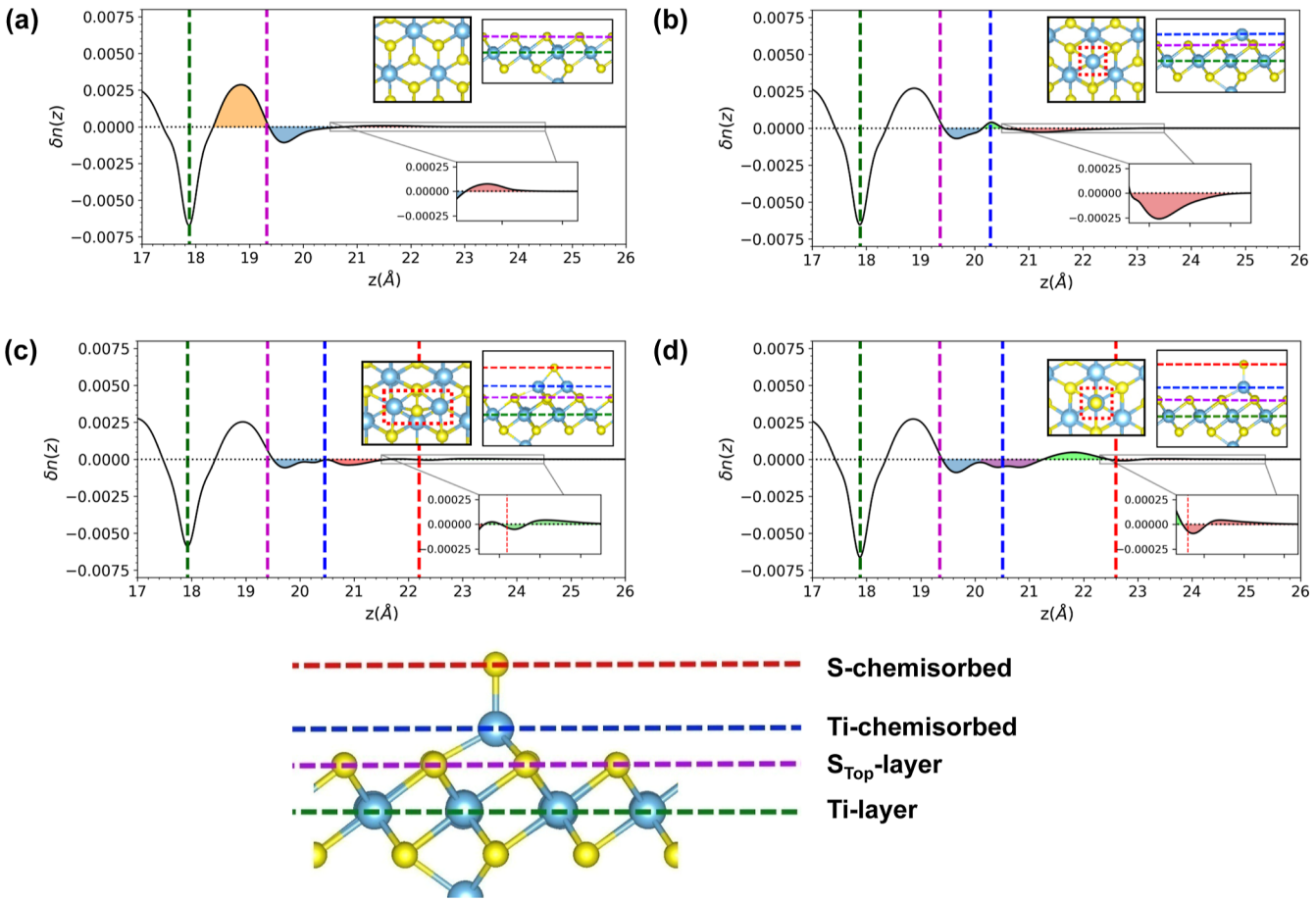

Figure 5. *xy*-plane-averaged electron difference density ($\delta n(z)$) of $Ti_{1.031}S_2$ with (a) pristine surface and with a surface chemisorbed with adparticles X = (b) Ti, (c) Ti_2S, and (d) TiS. The top view and side view of the adsorption structures are shown as insets in the corresponding figure panel. Positive/negative $\delta n(z)$ represents enhanced/suppressed electron density. The heights of the Ti-layer, S_{Top}-layer, chemisorbed Ti atom(s), and chemisorbed S atom are indicated by green, magenta, blue, and red dashed lines, respectively. A schematic of the TiS-chemisorbed surface configuration is shown at the bottom of the figure for reference.

When highly electropositive adparticles (Ti or Ti_2S) are chemisorbed on the surface of $Ti_{1.031}S_2$, they transfer electrons to the S_{top}-layer. This is evidenced by reduced depletion of $\delta n(z)$ between the S_{top}-layer and chemisorbed Ti atom(s) (blue region in Figure 5b,c) and formation of negative $\delta n(z)$ regions in the vacuum near the chemisorbed Ti atoms (red region in Figure 5b,c). According to eq 4, these negative $\delta n(z)$ regions would induce large positive electric dipoles, generating negative Φ_{vac}. The Φ_{vac} value of Ti_2S:$Ti_{1.031}S_2$ is more positive than that of Ti:$Ti_{1.031}S_2$ because the chemisorbed S atom receives electrons from chemisorbed Ti atoms, lessens the depletion of $\delta n(z)$ near the chemisorbed Ti atoms (red region in Figure 5c), and forms a small region of positive $\delta n(z)$ in a vacuum (green region in Figure 5d). For TiS:$Ti_{1.031}S_2$, the chemisorbed Ti atom transfers electrons to the atoms in the S_{top}-layer and the chemisorbed S atoms. This charge transfer reduces the depletion of $\delta n(z)$ (blue region in Figure 5d) between the S_{top}-layer and the chemisorbed Ti atom and creates a negative $\delta n(z)$ region centered around the chemisorbed Ti atom (purple region in Figure 5d) and a positive $\delta n(z)$ region right below the chemisorbed S atom (green region in Figure 5d). Subsequently, the positive $\delta n(z)$ region (green region in Figure 5c) repels electrons in its vicinity, creating a region of negative $\delta n(z)$, followed by a positive $\delta n(z)$ region extending in a vacuum (red region in Figure 5d). Thus, the high electronegativity of the chemisorbed S atom shifts the electron distribution outward, resulting in a positive Φ_{vac}.

3.4. Modulation of Work Function with Surface Oxidation. Although our results indicate the high formation energies would hinder the formation of S_V, previous experimental studies indicate that TiS_2 is highly susceptible to the oxidation process.[25,82] According to the results of molecular dynamics simulation,[83] a defect-free TiS_2 would hinder the oxidation process due to the high reaction energy barrier. However, the oxidation process would also facilitate the formation of sulfur vacancy (S_V) at the neighboring site; thus, an oxidation chain reaction can be initiated once the first S_V is present on the TiS_2 surface. In this section, a two-layer $Ti_{1.056}S_2$ slab is used as an underlying structure to study the surface oxidation process through formation energy calculations in Figure 6a. Sulfur atoms at the top surface layer are substituted with oxygen atoms (see Figure 7 for configurations with oxidized surfaces) with varying concentrations of oxidation until the surface is fully oxidized. For each concentration of oxidation, the positions of the substituted S atoms are randomly selected to generate 10 different configurations whenever possible.

We first calculate the oxidation formation energies (Figure 6a) of the oxidized $Ti_{1.056}S_2$ using eq 1, with the chemical

https://doi.org/10.1021/acsanm.5c03229
ACS Appl. Nano Mater. 2025, 8, 19840−19851

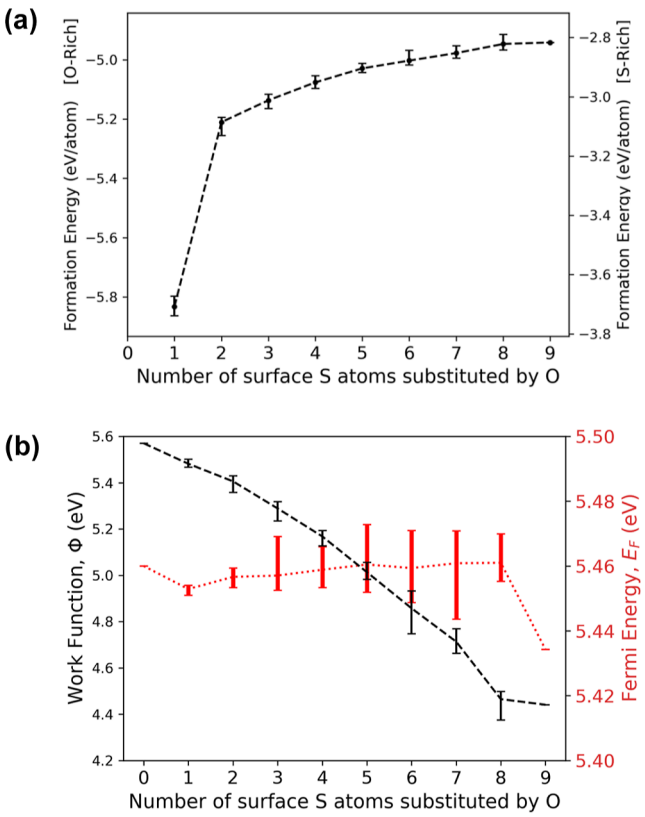

Figure 6. (a) Oxidation formation energies of $Ti_{1.056}S_2$ calculated using the PBE functional and (b) vacuum potential (Φ_{vac}) and Fermi energy (E_F) of $Ti_{1.056}S_2$ calculated using the HSE functional. Dashed lines represent the average values of the calculated quantities, while vertical solid lines indicate the range of calculated values.

potential of O set by the formation energy of O_2 gas. In general, the defect formation energy increases with the higher concentration of surface oxidation and is insensitive toward the positions of the chemisorbed O atoms. The average defect formation energy with 11.1% surface oxidation (when one S atom is substituted by O atom) is significantly lower than those with a higher concentration of surface oxidation, while the subsequent increase in surface oxidation would only slightly increase the defect formation energies.

Next, we calculated the work function of $Ti_{1.056}S_2$ as a function of surface oxidation concentration. $Ti_{1.056}S_2$ is chosen as the underlying structure to investigate surface oxidation since its theoretical lattice constant 10.18 Å in a 3 × 3 supercell well matches 10.07 Å in a 2 × 2 supercell of hexagonal titanium oxide Ti_2O_3.[84] Calculations using the HSE functional predict that the work function decreases with the increased concentration of surface oxidation (Figure 6b). The reduction of the work function is mainly attributed to the increasingly negative Φ_{vac}, while E_F remains relatively unchanged with the respective increasing concentration of surface oxidation.

In continuation, we plot $\delta n(z)$ of $Ti_{1.056}S_2$ surfaces with varying concentrations of surface oxidation and examine their percentage change in the electron number ($\int \delta n(z)dz$) across the S_{Bot}−Ti, Ti, Ti−S_{top}, S_{top}-Vac, and Vac regions in Figure 7. The notable results are summarized as follows:

i Electron number in the S_{Bot}-Ti region decreases as oxidation density rises. The reduction happens because Ti atom transfers a larger fraction of electrons to the increasing highly electronegative O atoms, leaving less electrons available to the Ti−S bond.

ii Electron number in the Ti region increases as oxidation density rises. On the other hand, the electron number in the Ti−S_{top} region shows a slight decrease when oxidation density rises to 33% but increases with further rises in oxidation density (>33%). These observations contrast with the Mulliken population analysis (see Table S3), which indicates that Ti (O) in the Ti−O bond exhibits significantly higher positive (negative) atomic charge compared to Ti (S) in the Ti−S bond. The contrast in these two analyses stems from the substantial overlap of Ti's and O's atomic charges along the z-axis due to the short vertical distance between Ti and O atoms.

iii Chemisorbed O atoms are positioned at lower vertical heights, owing to the shorter Ti−O bond length (range from 1.8 Å to 2.1 Å) compared to the Ti−S bond length (≈2.4 Å). As the density of oxidation increases, the peak of $\delta n(z)$ in the Ti−S_{top} region (purple regions in Figure 7 (a)-(d)) shifts toward the height of the O_{Top} layer. In the case of a fully oxidized surface, the peak of $\delta n(z)$ aligns closely with the average height of the oxygen atoms. Furthermore, the isosurface plot (see Figure S14) indicates that $\delta n(z)$ exhibits a sphere-like distribution around the oxygen atoms. This behavior suggests that the Ti−O bond has a more ionic character compared to the predominantly covalent nature of the Ti−S bond. Due to the covalency of Ti−S bond, the S atoms at the S_{Top}-layer transfer some of the electrons from the nearest vacuum (S_{top}-Vac region) to the Ti−S bonds, the depletion of which is accompanied by a slight increase of electrons in Vac regions. In contrast, the sphere-like distribution of excess electrons around the oxygen atoms induces a larger magnitude of electron depletion in the S_{top}-Vac region. As a result, the electron number in S_{top}-Vac and Vac regions decreases as oxidation density rises. Notably, the electron number in the Vac region nearly reduces to zero when the surface is fully oxidized.

iv. The total change in electron number must be zero; therefore, the reduction of electron number in S_{top}-Vac and Vac regions is accompanied by a corresponding increase of electron number in the lower oxygen regions. However, eq 4 indicates that the changes of $\delta n(z)$ in S_{top}-Vac and Vac regions carry more significant weightage in determining Φ_{vac} because of their higher vertical positions. Consequently, Φ_{vac} and the work function of $Ti_{1.056}S_2$ decrease as oxidation density rises.

Finally, we discuss the effect of Al_2O_3 substrate on the electronic structures of TiS_2 in the Supporting Information. The lattice and band structures of bulk α-Al_2O_3 are shown in Figure S1 for reference. We begin with examining the stability of various surface terminations of the Al_2O_3 substrate (Figures S2−S4). The total energy listed in Table S1 shows that Type-IV structure (Figure S4) is the most stable lattice structure. The band structures of the corresponding thin films are depicted in Figure S5. We then investigate the adsorption energy (Table S2) of Ti, S, Al, O, and N atoms at the top- and hollow-site on the Al_2O_3 surface (Figure S6), indicating that Ti exhibits the most stable adsorption among all. We also analyze the band structure and work function of TiS_2 with different thicknesses on the Al_2O_3 substrate. As shown in Figure S7, for

https://doi.org/10.1021/acsanm.5c03229
ACS Appl. Nano Mater. 2025, 8, 19840−19851

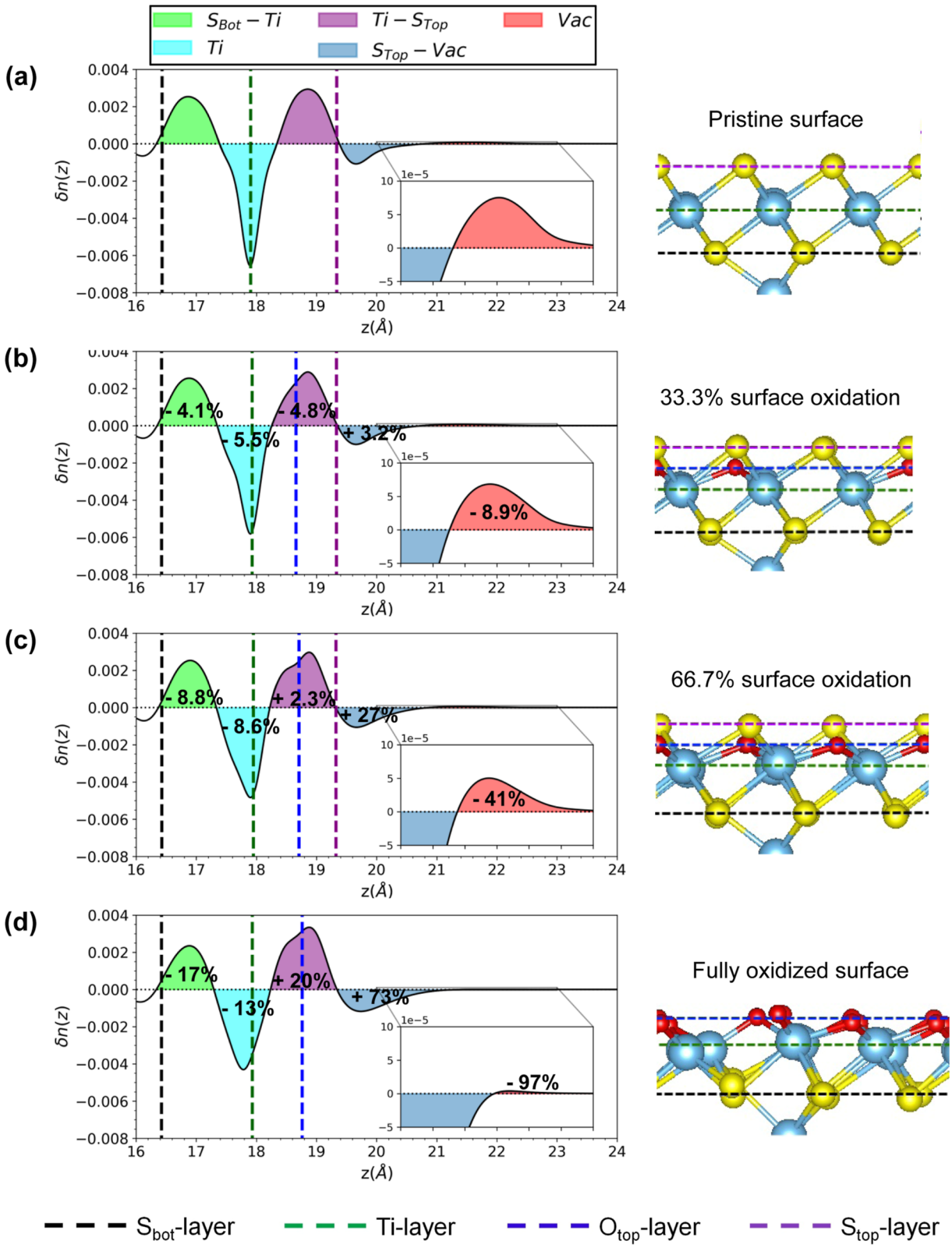

Figure 7. *xy*-plane-averaged electron difference density ($\delta n(z)$) of $Ti_{1.047}S_2$ for (a) pristine surface and surfaces with (b) 33%, (c) 66%, and (d) 100% oxidation. Positive/negative $\delta n(z)$ represents enhanced/suppressed electron density. The percentage changes of absolute value of integrated electron difference density ($\int \delta n(z)dz$) compared to pristine surface are shown for the S_{Bot}−Ti, Ti, Ti−S_{Top}, S_{Top}-Vac, and Vac regions. The heights of the S_{Bot}-layer, Ti-layer, O_{Top}-layer, and S_{Top}-layer are indicated by black, green, blue, and magenta dashed lines, respectively. A schematic of the oxidized $Ti_{1.047}S_2$ surface configuration is shown at the bottom of the figure for reference.

1−4 layers of TiS_2 on top of Al_2O_3, the bands near the Fermi level are predominantly contributed by TiS_2, implying that electrons are transferred from Al_2O_3. However, the work function does not significantly change with increasing

https://doi.org/10.1021/acsanm.5c03229
ACS Appl. Nano Mater. 2025, 8, 19840−19851

thickness. With TiS_2 multilayers on top of Al_2O_3, slight lattice compression and interfacial charge transfer occur. This interfacial charge transfer is identified as the main reason for the notable increase in work function compared to pristine TiS_2 (Figures S8 and S9). We further analyze the effect of Ti intercalation on the system's work function. The results in Figure S10 show that, regardless of the presence of Ti intercalants, a redistribution of charge density occurs at the TiS_2/Al_2O_3 interface, which is the key factor driving the variation in work function.

4. CONCLUSIONS

In this work, DFT calculations were used to calculate the effect of defects and thickness toward the work function of TiS_2. We identify a number of key findings, which are important to understand the engineering of work function of TiS_2:

i. This experimental trend—where the pristine sample exhibits a significantly higher work function (5.3 eV[34]) than the oxidized one (4.13 eV[49])—provides strong qualitative support for our theoretical calculation work functions. Specifically, our calculations show that TiS_2 with a pristine surface has work function ranging from 5.55 to 5.75 eV; with an increasing density of surface oxidation concentration, the calculated work function decreases to 4.45 eV.

ii. The presence of interstitial Ti would lower the work function of TiS_2 by 0.2−0.3 eV, depending on the concentration of Ti_i. It is crucial to understand the relationship between Ti_i's concentration and TiS_2's work function because Ti_i is the major electron donor of TiS_2.

iii. The chemisorption of adparticles consists of Ti atoms that have negative formation energies at Ti-rich conditions. This chemisorption would drastically alter the work function of TiS_2: less-electronegative adparticles Ti and Ti_2S lower the work function to 4.74 and 5.03 eV, respectively, whereas high-electronegative adparticle TiS increases the work function to 5.87 eV.

iv. The Al_2O_3 substrate increases the work function of TiS_2 up to 6.13 eV, and this effect is independent of the number of layers. However, the intercalation of Ti and Al atoms slightly reduces the work function.

Overall, this work suggests that the low measured work function of TiS_2 in experiments can be attributed to surface defects or surface oxidation. TiS_2 with a Ti_i defect shows metallic properties. When the surface is nearly defect-free, TiS_2 shows a remarkably large work function of 6.13 eV (5.94 eV) with (without) Al_2O_3 substrate. Furthermore, the work function is only slightly dependent on the film thickness and concentration of Ti_i, demonstrating TiS_2's potential as a high work function electrode.

■ ASSOCIATED CONTENT

Supporting Information

The Supporting Information is available free of charge at https://pubs.acs.org/doi/10.1021/acsanm.5c03229.

Lattice structures and band structures of bulk and slab Al_2O_3; total energies and band structures of slab Al_2O_3 with different terminations; adsorption lattice structures and total energies; lattice structures and band structures of TiS_2/Al_2O_3; work function of TiS_2, with doping, with strain, on top of Al_2O_3; charge distribution of TiS_2/Al_2O_3; charge analysis of surface oxidation; TiS_2 vacancy lattice structures; thickness-dependent band gap of TiS_2; defected TiS_2 lattice structures; charge analysis of defected TiS_2; and molecular dynamics of defected TiS_2 work function (PDF)

■ AUTHOR INFORMATION

Corresponding Author

Horng-Tay Jeng − *Department of Physics, National Tsing Hua University, Hsinchu 30013, Taiwan; Physics Division, National Center for Theoretical Sciences, Taipei 10617, Taiwan; Institute of Physics, Academia Sinica, Taipei 11529, Taiwan; Research Center for Semiconductor Materials and Advanced Optics, Chung Yuan Christian University, Taoyuan 32031, Taiwan;* orcid.org/0000-0002-2881-3826; Email: jeng@phys.nthu.edu.tw

Authors

Yee-Heng Teh − *Department of Physics, National Tsing Hua University, Hsinchu 30013, Taiwan*

Sheng-Hsiung Hung − *Department of Physics, National Tsing Hua University, Hsinchu 30013, Taiwan*

Chin-Hsuan Chen − *Department of Physics, National Tsing Hua University, Hsinchu 30013, Taiwan*

Angus Huang − *Department of Physics, National Tsing Hua University, Hsinchu 30013, Taiwan*

Jer-Fu Wang − *Corporate Research, Taiwan Semiconductor Manufacturing Company, Hsinchu 30091, Taiwan*

Chih-Piao Chuu − *Corporate Research, Taiwan Semiconductor Manufacturing Company, Hsinchu 30091, Taiwan*

Complete contact information is available at: https://pubs.acs.org/10.1021/acsanm.5c03229

Notes

The authors declare no competing financial interest.

■ ACKNOWLEDGMENTS

This work was supported by the National Science and Technology Council (NSTC), Taiwan. H.-T.J. also acknowledges support from NCHC, CINC-NTU, TSRI, AS-iMATE-111-12, and CQT-NTHU-MOE, Taiwan.

■ REFERENCES

(1) Wenger, C.; Lukosius, M.; Weidner, G.; Müssig, H. J.; Pasko, S.; Lohe, C. The role of the hfo2tin interface in capacitancevoltage nonlinearity of metal-insulator-metal capacitors. *Thin Solid Films* **2009**, *517* (23), 6334−6336 Proceedings on the Sixth Symposium on Thin Films for Large Area Electronics.

(2) Jeong, S.-W.; Lee, H.; Kim, K.; You, M.; Roh, Y.; Noguchi, T.; Xianyu, W.; Jung, J. Effects of annealing temperature on the characteristics of ald-deposited hfo2 in mim capacitors. *Thin Solid Films* **2006**, *515* (2), 526−530 Proceedings of the Eighth International Conference on Atomically Controlled Surfaces, Interfaces and Nanostructures and the Thirteenth International Congress on Thin Films.

(3) Perng, T.-H.; Chien, C.-H.; Chen, C.-W.; Lehnen, P.; Chang, C.-Y. High-density mim capacitors with hfo2 dielectrics. *Thin Solid Films* **2004**, *469−470*, 345−349 Proceedings of the 31st International Conference on Metallurgical Coatings and Thin Films.

(4) Hu, H.; Zhu, C.; Lu, Y.; Li, M.; Cho, B. J.; Choi, W. A high performance mim capacitor using hfo2 dielectrics. *IEEE Electron Device Lett.* **2002**, *23* (9), 514−516.

(5) Wenger, C.; Lukosius, M.; Müssig, H. J.; Ruhl, G.; Pasko, S.; Lohe, C. Influence of the electrode material on hfo2 metal-insulator-

metal capacitors. *J. Vac. Sci. Technol., B:Nanotechnol. Microelectron.:Mater., Process., Meas., Phenom.* **2009**, *27*, 286−289.
(6) Xiong, L.; Hu, J.; Yang, Z.; Li, X.; Zhang, H.; Zhang, G. Dielectric properties investigation of metalinsulatormetal (mim) capacitors. *Molecules* **2022**, *27* (12), 3951.
(7) Woo, J.-C.; Chun, Y.-S.; Joo, Y.-H.; Kim, C.-I. Low leakage current in metal-insulator-metal capacitors of structural al2o3/tio2/al2o3 dielectrics. *Appl. Phys. Lett.* **2012**, *100*, 081101.
(8) Chaker, A.; Gonon, P.; Valle, C.; Bsiesy, A. High capacitance density of 185 nF/mm2 achieved in three-dimensional MIM structures using TiO2 as a dielectric. *Appl. Phys. Lett.* **2017**, *110*, 243501.
(9) Cheng, C. H.; Lin, S. H.; Jhou, K. Y.; Chen, W. J.; Chou, C. P.; Yeh, F. S.; Hu, J.; Hwang, M.; Arikado, T.; McAlister, S. P.; Chin, A. High density and low leakage current in TiO_2 mim capacitors processed at 300 °C. *IEEE Electron Device Lett.* **2008**, *29* (8), 845−847.
(10) Du, L.; Wong, H.; Dong, S.; Lau, W.-S.; Filip, V. Afm study on the surface morphologies of tin films prepared by magnetron sputtering and al2o3 films prepared by atomic layer deposition. *Vacuum* **2018**, *153*, 139−144.
(11) Hudec, B.; Huekov, K.; Tarre, A.; Han, J. H.; Han, S.; Rosov, A.; Lee, W.; Kasikov, A.; Song, S. J.; Aarik, J.; Hwang, C. S.; Frhlich, K. Electrical properties of tio2-based mim capacitors deposited by ticl4 and ttip based atomic layer deposition processes. *Microelectron. Eng.* **2011**, *88* (7), 1514−1516 Proceedings of the 17th Biennial International Insulating Films on Semiconductor Conference.
(12) Robertson, J.; Wallace, R. M. High-k materials and metal gates for cmos applications. *Mater. Sci. Eng., R* **2015**, *88*, 1−41.
(13) Takeuchi, H.; Wong, H. Y.; Ha, D.; King, T.-J. Impact of oxygen vacancies on high-/spl kappa/gate stack engineering. In *IEDM Technical Digest. IEEE International Electron Devices Meeting, 2004*, 2004, pp 829−832.
(14) Datta, S.; Dewey, G.; Doczy, M.; Doyle, B.; Jin, B.; Kavalieros, J.; Kotlyar, R.; Metz, M.; Zelick, N.; Chau, R. High mobility si/sige strained channel mos transistors with hfo/sub 2//tin gate stack. In *IEEE International Electron Devices Meeting 2003*, 2003, pp 2811−2814.
(15) Dadgour, H. F.; Endo, K.; De, V. K.; Banerjee, K. "Grain-orientation induced work function variation in nanoscale metal-gate transistors"part i: Modeling, analysis, and experimental validation. *IEEE Trans. Electron Devices* **2010**, *57* (10), 2504−2514.
(16) Narula, V.; Agarwal, M.; Verma, S. A pathway to improve short channel effects of junctionless based fets after incorporating technology boosters: a review. *Eng. Res. Express* **2024**, *6*, 012301.
(17) Chen, J.; Sun, M.-Y.; Wang, Z.-H.; Zhang, Z.; Zhang, K.; Wang, S.; Zhang, Y.; Wu, X.; Ren, T.-L.; Liu, H.; Han, L. Performance limits and advancements in single 2d transition metal dichalcogenide transistor. *Nano-Micro Lett.* **2024**, *16*, 264.
(18) Liu, Y.; Duan, X.; Shin, H.-J.; Park, S.; Huang, Y.; Duan, X. Promises and prospects of two-dimensional transistors. *Nature* **2021**, *591*, 43−53.
(19) Chhowalla, M.; Jena, D.; Zhang, H. Two-dimensional semiconductors for transistors. *Nat. Rev. Mater.* **2016**, *1*, 16052.
(20) Zhang, J.; Liu, L.; Yang, Y.; Huang, Q.; Li, D.; Zeng, D. A review on two-dimensional materials for chemiresistive- and fet-type gas sensors. *Phys. Chem. Chem. Phys.* **2021**, *23*, 15420−15439.
(21) Schwierz, F.; Pezoldt, J.; Granzner, R. Two-dimensional materials and their prospects in transistor electronics. *Nanoscale* **2015**, *7*, 8261−8283.
(22) Nie, C.; Zhang, B.; Gao, Y.; Yin, M.; Yi, X.; Zhao, C.; Zhang, Y.; Luo, L.; Wang, S. Thickness-dependent enhancement of electronic mobility of mos2 transistors via surface functionalization. *J. Phys. Chem. C* **2020**, *124* (31), 16943−16950.
(23) Urade, A. R.; Lahiri, I.; Suresh, K. S. Graphene properties, synthesis and applications: A review. *JOM* **2023**, *75*, 614−630.
(24) Chen, Y.; Gong, X.-L.; Gai, J.-G. Progress and challenges in transfer of large-area graphene films. *Advanced Science* **2016**, *3* (8), 1500343.
(25) Chen, K.; Song, M.; Sun, Y.-Y.; Xu, H.; Qi, D.-C.; Su, Z.; Gao, X.; Xu, Q.; Hu, J.; Zhu, J.; Zhang, R.; Wang, J.; Zhang, L.; Cao, L.; Han, Y.; Xiong, Y. Defects controlled doping and electrical transport in tis2 single crystals. *Appl. Phys. Lett.* **2020**, *116*, 121901.
(26) Gao, Z.; Ji, Q.; Shen, P.-C.; Han, Y.; Leong, W. S.; Mao, N.; Zhou, L.; Su, C.; Niu, J.; Ji, X.; Goulamaly, M. M.; Muller, D. A.; Li, Y.; Kong, J. In situ-generated volatile precursor for cvd growth of a semimetallic 2d dichalcogenide. *ACS Appl. Mater. Interfaces* **2018**, *10* (40), 34401−34408.
(27) Hu, Z.; Tai, Z.; Liu, Q.; Wang, S.-W.; Jin, H.; Wang, S.; Lai, W.; Chen, M.; Li, L.; Chen, L.; Tao, Z.; Chou, S.-L. Ultrathin 2d tis2 nanosheets for high capacity and long-life sodium ion batteries. *Adv. Energy Mater.* **2019**, *9* (8), 1803210.
(28) Alvarez Ferrero, G.; vall, G.; Mazzio, K. A.; Son, Y.; JanÃŸen, K.; Risse, S.; Adelhelm, P. Co-intercalation batteries (coibs): Role of tis2 as electrode for storing solvated na ions. *Adv. Energy Mater.* **2022**, *12* (47), 2202377.
(29) Park, J.; Kim, S. J.; Lim, K.; Cho, J.; Kang, K. Reconfiguring sodium intercalation process of tis2 electrode for sodium-ion batteries by a partial solvent cointercalation. *ACS Energy Lett.* **2022**, *7* (10), 3718−3726.
(30) Oh, D. Y.; Choi, Y. E.; Kim, D. H.; Lee, Y.-G.; Kim, B.-S.; Park, J.; Sohn, H.; Jung, Y. S. All-solid-state lithium-ion batteries with tis2 nanosheets and sulphide solid electrolytes. *J. Mater. Chem. A* **2016**, *4*, 10329−10335.
(31) Shin, B. R.; Nam, Y. J.; Oh, D. Y.; Kim, D. H.; Kim, J. W.; Jung, Y. S. Comparative study of tis2/li-in all-solid-state lithium batteries using glass-ceramic li3ps4 and li10gep2s12 solid electrolytes. *Electrochim. Acta* **2014**, *146*, 395−402.
(32) Zhang, R.; Yang, X.; Xu, S.; Xu, D.; Du, F. A kinetics study on intercalation pseudocapacitance of layered tis2 in k-ion batteries. *Phys. Chem. Chem. Phys.* **2019**, *21*, 25940−25944.
(33) Sun, X.; Bonnick, P.; Nazar, L. F. Layered tis2 positive electrode for mg batteries. *ACS Energy Lett.* **2016**, *1* (1), 297−301.
(34) Di, B.; Li, X.; Wen, X.; Lei, W.; Xu, X.; Kong, W.; Chang, H.; Zhang, J.; Zhang, W. High-quality p-type contacts for atomically thin mote2 transistors with high-work-function semimetal tis2 electrodes. *ACS Appl. Mater. Interfaces* **2025**, *17* (17), 25518−25525.
(35) Miao, J.; Zhang, H.; Bian, Z.; Zhang, T.; Zhao, Y. Boosting 2d transistor performance via tis2 van der waals contact engineering. In *2025 9th IEEE Electron Devices Technology & Manufacturing Conference (EDTM)*, 2025, pp 1−3.
(36) Liu, Y.; Stradins, P.; Wei, S.-H. Van der waals metal-semiconductor junction: Weak fermi level pinning enables effective tuning of schottky barrier. *Sci. Adv.* **2016**, *2* (4), No. e1600069.
(37) Shen, P.-C.; Su, C.; Lin, Y.; Chou, A.-S.; Cheng, C.-C.; Park, J.-H.; Chiu, M.-H.; Lu, A.-Y.; Tang, H.-L.; Tavakoli, M. M.; Pitner, G.; Ji, X.; Cai, Z.; Mao, N.; Wang, J.; Tung, V.; Li, J.; Bokor, J.; Zettl, A.; Wu, C.-I.; Palacios, T.; Li, L.-J.; Kong, J. Ultralow contact resistance between semimetal and monolayer semiconductors. *Nature* **2021**, *593*, 211−217.
(38) Liu, X.; Choi, M. S.; Hwang, E.; Yoo, W. J.; Sun, J. Fermi level pinning dependent 2d semiconductor devices: Challenges and prospects. *Adv. Mater.* **2022**, *34* (15), 2108425.
(39) Ngo, T. D.; Huynh, T.; Jung, H.; Ali, F.; Jeon, J.; Choi, M. S.; Yoo, W. J. Modulation of contact resistance of dual-gated mos2 fets using fermi-level pinning-free antimony semi-metal contacts. *Advanced Science* **2023**, *10* (21), 2301400.
(40) Wang, H.; Qiu, Z.; Xia, W.; Ming, C.; Han, Y.; Cao, L.; Lu, J.; Zhang, P.; Zhang, S.; Xu, H.; Sun, Y.-Y. Semimetal or semiconductor: The nature of high intrinsic electrical conductivity in tis2. *J. Phys. Chem. Lett.* **2019**, *10* (22), 6996−7001.
(41) Das, T.; Chakraborty, S.; Ahuja, R.; Das, G. P. Tis2 monolayer as an emerging ultrathin bifunctional catalyst: Influence of defects and functionalization. *ChemPhysChem* **2019**, *20* (4), 608−617.
(42) Liu, Y.; Kijima, S.; Sugimata, E.; Masahara, M.; Endo, K.; Matsukawa, T.; Ishii, K.; Sakamoto, K.; Sekigawa, T.; Yamauchi, H.; Takanashi, Y.; Suzuki, E. Investigation of the tin gate electrode with

tunable work function and its application for finfet fabrication. *IEEE Trans. Nanotechnol.* **2006**, *5* (6), 723−730.
(43) Li, G.; Zimmermann, T.; Cao, Y.; Lian, C.; Xing, X.; Wang, R.; Fay, P.; Xing, H. G.; Jena, D. Threshold voltage control in $Al_{0.72}Ga_{0.28}N$/AlN/GaN hemts by work-function engineering. *IEEE Electron Device Lett.* **2010**, *31* (9), 954−956.
(44) Javey, A.; Guo, J.; Wang, Q.; Lundstrom, M.; Dai, H. Ballistic carbon nanotube field-effect transistors. *Nature* **2003**, *424*, 654−657.
(45) Zhao, Y.; Nardes, A. M.; Zhu, K. Effective hole extraction using moox-al contact in perovskite ch3nh3pbi3 solar cells. *Appl. Phys. Lett.* **2014**, *104*, 213906.
(46) Fang, H.; Chuang, S.; Chang, T. C.; Takei, K.; Takahashi, T.; Javey, A. High-performance single layered wse2 p-fets with chemically doped contacts. *Nano Lett.* **2012**, *12* (7), 3788−3792.
(47) Schulz, P.; Tiepelt, J. O.; Christians, J. A.; Levine, I.; Edri, E.; Sanehira, E. M.; Hodes, G.; Cahen, D.; Kahn, A. High-work-function molybdenum oxide hole extraction contacts in hybrid organicinorganic perovskite solar cells. *ACS Appl. Mater. Interfaces* **2016**, *8* (46), 31491−31499.
(48) Chuang, S.; Battaglia, C.; Azcatl, A.; McDonnell, S.; Kang, J. S.; Yin, X.; Tosun, M.; Kapadia, R.; Fang, H.; Wallace, R. M.; Javey, A. Mos2 p-type transistors and diodes enabled by high work function moox contacts. *Nano Lett.* **2014**, *14* (3), 1337−1342.
(49) Huckaba, A. J.; Gharibzadeh, S.; Ralaiarisoa, M.; Roldán-Carmona, C.; Mohammadian, N.; Grancini, G.; Lee, Y.; Amsalem, P.; Plichta, E. J.; Koch, N.; Moshaii, A.; Nazeeruddin, M. K. Low-cost tis2 as hole-transport material for perovskite solar cells. *Small Methods* **2017**, *1* (10), 1700250.
(50) Kovarik, L.; Bowden, M.; Szanyi, J. High temperature transition aluminas in δ-Al2O3/θ-Al2O3 stability range: Review. *J. Catal.* **2021**, *393*, 357−368.
(51) Schmaljohann, F.; Hagedorn, D.; Lffler, F. Electrical insulation performance of aluminum oxide layers on metallic substrates − HiPIMS compared to RF-MS. *Surf. Coat. Technol.* **2019**, *361*, 119−122.
(52) Tran, G. T.; Nguyen, N. T. H.; Nguyen, N. T. T.; Nguyen, T. T. T.; Nguyen, D. T. C.; Tran, T. V. Plant extract-mediated synthesis of aluminum oxide nanoparticles for water treatment and biomedical applications: a review. *Environ. Chem. Lett.* **2023**, *21*, 2417−2439.
(53) Groven, B.; Mehta, A. N.; Bender, H.; Smets, Q.; Meersschaut, J.; Franquet, A.; Conard, T.; Nuytten, T.; Verdonck, P.; Vandervorst, W.; Heyns, M.; Radu, I.; Caymax, M.; Delabie, A. Nucleation mechanism during ws2 plasma enhanced atomic layer deposition on amorphous al2o3 and sapphire substrates. *J. Vac. Sci. Technol., A* **2018**, *36*, 01A105.
(54) Schilir, E.; Panasci, S.; Mio, A.; Nicotra, G.; Agnello, S.; Pecz, B.; Radnoczi, G.; Deretzis, I.; Magna, A. L.; Roccaforte, F.; Nigro, R. L.; Giannazzo, F. Direct atomic layer deposition of ultra-thin Al2O3 and HfO2 films on gold-supported monolayer MoS2. *Appl. Surf. Sci.* **2023**, *630*, 157476.
(55) Schilirò, E.; Nigro, R. L.; Panasci, S. E.; Agnello, S.; Cannas, M.; Gelardi, F. M.; Roccaforte, F.; Giannazzo, F. Direct atomic layer deposition of ultrathin aluminum oxide on monolayer mos2 exfoliated on gold: The role of the substrate. *Adv. Mater. Interfaces* **2021**, *8*, 2101117.
(56) Huang, B.; Zheng, M.; Zhao, Y.; Wu, J.; Thong, J. T. L. Atomic layer deposition of high-quality al2o3 thin films on mos2 with water plasma treatment. *ACS Appl. Mater. Interfaces* **2019**, *11*, 35438−35443.
(57) Lin, Z.; Wu, X.; Cott, D.; Shi, Y.; Silva, H. M.; Sergeant, S.; Conard, T.; Meersschaut, J.; Mehta, A. N.; Groven, B.; Morin, P.; Asselberghs, I.; de la Rosa, C. J. L.; Kar, G. S.; Lin, D.; Delabie, A. Top-gate stack engineering featuring a high- gadolinium aluminate interfacial layer for field-effect transistors based on two-dimensional transition-metal dichalcogenides. *ACS Appl. Electron. Mater.* **2024**, *6*, 4213−4222.
(58) Bisht, P.; Shim, J.; Oh, J.; Lee, J.; Shin, H.; Jeong, H.; Kim, J.; Lee, J.; Kwon, H.-J.; Kim, S. Next generation high-mobility 2d chalcogenides tft for display backplane. *Int. J. Extreme Manuf.* **2025**, *7*, 052005.
(59) Das, S.; Chowdhury, R. K.; Karmakar, D.; Das, S.; Ray, S. K. Substrate-dependent synergistic many-body effects in atomically thin two-dimensional ws2. *Phys. Rev. Mater.* **2021**, *5*, 124001.
(60) Zhu, H.; Addou, R.; Wang, Q.; Nie, Y.; Cho, K.; Kim, M.; Wallace, R. Surface and interfacial study of atomic layer deposited al2o3 on mote2 and wte2. *Nanotechnology* **2020**, *31*, 055704.
(61) Smidstrup, S.; Markussen, T.; Vancraeyveld, P.; Wellendorff, J.; Schneider, J.; Gunst, T.; Verstichel, B.; Stradi, D.; Khomyakov, P. A.; Vej-Hansen, U. G.; Lee, M.-E.; Chill, S. T.; Rasmussen, F.; Penazzi, G.; Corsetti, F.; Ojanperä, A.; Jensen, K.; Palsgaard, M. L. N.; Martinez, U.; Blom, A.; Brandbyge, M.; Stokbro, K. Quantumatk: an integrated platform of electronic and atomic-scale modelling tools. *J. Phys.: Condens. Matter* **2020**, *32*, 015901.
(62) Hamann, D. R. Optimized norm-conserving vanderbilt pseudopotentials. *Phys. Rev. B* **2013**, *88*, 085117.
(63) Perdew, J. P.; Burke, K.; Ernzerhof, M. Generalized gradient approximation made simple. *Phys. Rev. Lett.* **1996**, *77*, 3865−3868.
(64) Grimme, S. Semiempirical gga-type density functional constructed with a long-range dispersion correction. *J. Comput. Chem.* **2006**, *27* (15), 1787−1799.
(65) Krukau, A. V.; Vydrov, O. A.; Izmaylov, A. F.; Scuseria, G. E. Influence of the exchange screening parameter on the performance of screened hybrid functionals. *J. Chem. Phys.* **2006**, *125*, 224106.
(66) Guidon, M.; Hutter, J.; VandeVondele, J. Auxiliary density matrix methods for hartree'fock exchange calculations. *J. Chem. Theory Comput.* **2010**, *6* (8), 2348−2364.
(67) Kresse, G.; Hafner, J. Ab initio molecular dynamics for liquid metals. *Phys. Rev. B* **1993**, *47*, 558.
(68) Kresse, G.; Furthmller, J. Efficiency of ab-initio total energy calculations for metals and semiconductors using a plane-wave basis set. *Comput. Mater. Sci.* **1996**, *6*, 15−50.
(69) Kasai, H.; Tolborg, K.; Sist, M.; Zhang, J.; Hathwar, V. R.; Filsø, M. Ø.; Cenedese, S.; Sugimoto, K.; Overgaard, J.; Nishibori, E.; Iversen, B. B. X-ray electron density investigation of chemical bonding in van der waals materials. *Nat. Mater.* **2018**, *17*, 249−252.
(70) Xu, C.; Brown, P. A.; Shuford, K. L. Strain-induced semimetal-to-semiconductor transition and indirect-to-direct band gap transition in monolayer 1t-tis2. *RSC Adv.* **2015**, *5*, 83876−83879.
(71) Freysoldt, C.; Grabowski, B.; Hickel, T.; Neugebauer, J.; Kresse, G.; Janotti, A.; Van de Walle, C. G. First-principles calculations for point defects in solids. *Rev. Mod. Phys.* **2014**, *86*, 253−305.
(72) O'Hare, P.; Johnson, G. Thermochemistry of inorganic sulfur compounds vii. standard molar enthalpy of formation at 298.15 k, high-temperature enthalpy increments, and other thermodynamic properties to 1100 k of titanium disulfide, tis2. *J. Chem. Thermodyn.* **1986**, *18* (2), 189−199.
(73) Paier, J.; Marsman, M.; Hummer, K.; Kresse, G.; Gerber, I. C.; Ángyán, J. G. Screened hybrid density functionals applied to solids. *J. Chem. Phys.* **2006**, *124*, 154709.
(74) Heyd, J.; Scuseria, G. E.; Ernzerhof, M. Hybrid functionals based on a screened coulomb potential. *J. Chem. Phys.* **2003**, *118*, 8207−8215.
(75) Kim, Y.-S.; Hummer, K.; Kresse, G. Accurate band structures and effective masses for inp, inas, and insb using hybrid functionals. *Phys. Rev. B* **2009**, *80*, 035203.
(76) Heyd, J.; Scuseria, G. E.; Ernzerhof, M. Erratum: "Hybrid functionals based on a screened Coulomb potential" [J. Chem. Phys. 118, 8207 (2003)]. *J. Chem. Phys.* **2006**, *124*, 219906.
(77) Perdew, J. P.; Ernzerhof, M.; Burke, K. Rationale for mixing exact exchange with density functional approximations. *J. Chem. Phys.* **1996**, *105*, 9982−9985.
(78) Alkauskas, A.; Broqvist, P.; Pasquarello, A. Defect levels through hybrid density functionals: Insights and applications. *Phys. Status Solidi B* **2011**, *248* (4), 775−789.

https://doi.org/10.1021/acsanm.5c03229
ACS Appl. Nano Mater. 2025, 8, 19840−19851

(79) Marques, M. A. L.; Vidal, J.; Oliveira, M. J. T.; Reining, L.; Botti, S. Density-based mixing parameter for hybrid functionals. *Phys. Rev. B* **2011**, *83*, 035119.
(80) Smoluchowski, R. Anisotropy of the electronic work function of metals. *Phys. Rev.* **1941**, *60*, 661−674.
(81) Leung, T. C.; Kao, C. L.; Su, W. S.; Feng, Y. J.; Chan, C. T. Relationship between surface dipole, work function and charge transfer: Some exceptions to an established rule. *Phys. Rev. B* **2003**, *68*, 195408.
(82) Long, E.; O'Brien, S.; Lewis, E. A.; Prestat, E.; Downing, C.; Cucinotta, C. S.; Sanvito, S.; Haigh, S. J.; Nicolosi, V. An in situ and ex situ tem study into the oxidation of titanium (iv) sulphide. *npj 2D Mater. Appl.* **2017**, *1*, 22.
(83) Cucinotta, C. S.; Dolui, K.; Pettersson, H.; Ramasse, Q. M.; Long, E.; O'Brian, S. E.; Nicolosi, V.; Sanvito, S. Electronic properties and chemical reactivity of tis2 nanoflakes. *J. Phys. Chem. C* **2015**, *119* (27), 15707−15715.
(84) Yoshimatsu, K.; Hasegawa, N.; Nambu, Y.; Ishii, Y.; Wakabayashi, Y.; Kumigashira, H. Metallic ground states of undoped ti2o3 films induced by elongated c-axis lattice constant. *Sci. Rep.* **2020**, *10*, 22109.

https://doi.org/10.1021/acsanm.5c03229
ACS Appl. Nano Mater. 2025, 8, 19840−19851